Reconstruction of Zebrafish Early Embryonic Development by Scanned Light Sheet Microscopy

Philipp J. Keller,[1,2]* Annette D. Schmidt,[2] Joachim Wittbrodt,[1,2,3,4]* Ernst H.K. Stelzer[1]

A long-standing goal of biology is to map the behavior of all cells during vertebrate embryogenesis. We developed digital scanned laser light sheet fluorescence microscopy and recorded nuclei localization and movement in entire wild-type and mutant zebrafish embryos over the first 24 hours of development. Multiview in vivo imaging at 1.5 billion voxels per minute provides "digital embryos," that is, comprehensive databases of cell positions, divisions, and migratory tracks. Our analysis of global cell division patterns reveals a maternally defined initial morphodynamic symmetry break, which identifies the embryonic body axis. We further derive a model of germ layer formation and show that the mesendoderm forms from one-third of the embryo's cells in a single event. Our digital embryos, with 55 million nucleus entries, are provided as a resource.

Model systems such as *Caenorhabditis elegans* and *Ciona intestinalis* lend themselves well to comprehensive analyses at the cellular level, for example, by conventional microscopy (*1*, *2*). However, global studies of complex vertebrate species encounter technical limitations. Whereas the formation of single organs has been reconstructed by imaging and tracking nuclear fluorescent proteins for several hours (*3*–*6*), obtaining quantitative morphogenetic data representing the full embryos over the entire time course of embryogenesis remains a major challenge.

For comparison, 671 cells need to be followed during *C. elegans* embryogenesis, whereas the analysis of complex vertebrate embryos requires the simultaneous tracking of tens of thousands of cells. High spatiotemporal resolution, ultralow photobleaching rates, and an excellent signal-to-noise ratio are crucial. In order to follow the nuclei of the 16,000 cells of an 18-hour-old zebrafish embryo, a volume of 1000 by 1000 by 1000 μm^3 must be recorded at least once every 90 s because nuclei move several micrometers per minute. In order to reliably detect all nuclei, the set of images must be acquired at a step size of no more than 3 μm along the *z* axis, resulting in ~350 images per time point. In addition, an image size of at least 1500 by 1500 pixels is necessary to elucidate nuclear morphologies. Thus, the observation must be performed at a continuous imaging speed of at least 10 million volume elements (voxels) per second. A dynamic range of at least 12 bit covers the varying expression levels of genetically encoded markers. At the same time, photobleaching and phototoxicity (*7*) must be minimized to ensure the physiological development of the embryo. Finally, the embryo's central yolk cell is opaque at physiological wavelengths; therefore, imaging along multiple directions is needed to capture the development of the entire embryo.

The most widely applied advanced fluorescence imaging techniques rely on confocal and multiphoton microscopes, which provide three-dimensional resolution but lack the combination of high-speed imaging and low phototoxicity required for the fast recording of entire embryos over long periods of time. They are also unsuited for multiview imaging (*8*). To overcome some of these limitations, we recently introduced light sheet–based technologies to biological imaging (SPIM) (*9*). With these microscopes, the specimen is illuminated along a single plane with a sheet of light that is typically generated via a set of apertures and by focusing a collimated beam with a cylindrical lens. This arrangement provides three-dimensional optical sectioning and reduces the energy load on the specimen (*9*–*11*).

Digital scanned laser light sheet fluorescence microscopy. To achieve the imaging speed and quality for recording entire embryos, we developed digital scanned laser light sheet fluorescence microscopy (DSLM) (fig. S1). The idea behind DSLM is to generate a "plane of light" with a laser scanner that rapidly moves a micrometer-thin beam of laser light vertically and horizontally through the specimen (Fig. 1 and movie S1).

This approach has several advantages over standard light sheet microscopy. First, DSLM illuminates each line in the specimen with the same intensity, a crucial prerequisite for quantitative imaging of large specimens (fig. S2). Second, in contrast to standard light sheet–based microscopy, DSLM does not rely on apertures to form the laser profile, which reduces optical aberrations and thereby provides an exceptional image quality. Third, the entire illumination power of the light source is focused into a single line, resulting in an illumination efficiency of 95% as compared with ~3% in standard light sheet microscopy. Fourth, DSLM allows to generate intensity-modulated illumination patterns (structured illumination) (*12*), which can be used to enhance the image contrast in highly light-scattering specimens, such as large embryos. Furthermore, DSLM combines (i) an imaging speed of 63 million voxels per second, (ii) a signal-to-noise ratio of 1000:1 at a lateral and axial resolution of 300 and 1000 nm, respectively, and (iii) ultralow excitation energies confined to a single plane (1.7 μJ at 488 nm passing each plane in our zebrafish experiments) (*8*).

In order to analyze zebrafish embryonic development, we recorded stacks of ~400 images (2048 by 2048 pixels each) in intervals of 60 or 90 s and along two opposing directions (Fig. 2 and movies S2 and S3). The embryos were embedded in agarose, kept at a constant temperature (26.5°C) [see (*13*) for developmental stages] throughout the experiment, and exhibited normal development (*8*). Nuclei were labeled at the one-cell stage by mRNA injection of H2B-eGFP, a fusion protein of human histone-2B and the en-

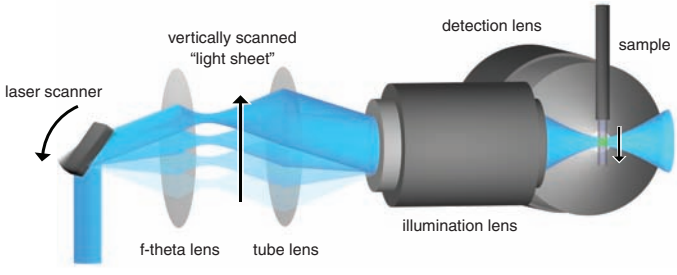

Fig. 1. Digital scanned laser light sheet microscopy. The laser beam illuminates the specimen from the side and excites fluorophores along a single line. Rapid scanning of a thin volume and fluorescence detection at a right angle to the illumination axis provides an optically sectioned image (movie S1). The f-theta lens converts the tilting movement of the scan mirror into a vertical displacement of the laser beam. The tube lens and the illumination objective focus the laser beam into the specimen, which is positioned in front of the detection lens.

[1]Cell Biology and Biophysics Unit, European Molecular Biology Laboratory (EMBL), Meyerhofstrasse 1, D-69117 Heidelberg, Germany. [2]Developmental Biology Unit, EMBL, Meyerhofstrasse 1, D-69117 Heidelberg, Germany. [3]Institute of Zoology, Department for Developmental Physiology, University of Heidelberg, INF 230, D-69120 Heidelberg, Germany. [4]Institute of Toxicology and Genetics, Karlsruhe Institute of Technology (KIT), Post Office Box 3640, D-76021 Karlsruhe, Germany.

*To whom correspondence should be addressed. E-mail: keller@embl.de (P.J.K.), wittbrod@embl.de (J.W.)

hanced green fluorescent protein (GFP) reporter, which localizes to chromatin (*14*). This presents an effective marker for cell positions and cell divisions because changes in chromatin density can be directly observed. Imaging was performed for 24 hours, providing about 400,000 images per embryo.

We measured nuclear fluorescence intensities and found that steady-state GFP concentrations are reached at ~12 hours post fertilization (hpf), owing to the limited stability of the injected mRNA. However, despite continuous imaging for another 12 hours, the fluorescence intensity levels remained constant. This indicates a negligible photobleaching rate in DSLM high-speed live imaging (fig. S3). We applied comparable experimental settings in state-of-the-art confocal and two-photon fluorescence microscopes. The embryo was exposed to a factor of 5600 more energy in the confocal (9.6 mJ at 488 nm passing each plane) and to a factor of 10^6 more energy in the two-photon fluorescence microscope (1.7 J at 930 nm passing each plane) (*8*). Thus, DSLM allows for a comprehensive, quantitative analysis of zebrafish embryonic development, over periods longer than 24 hours, with high spatiotemporal resolution and ultralow phototoxicity.

The digital embryo. To efficiently handle the large amounts of microscopy data, we developed a parallelized image segmentation pipeline, i.e., a set of software modules that automatically detects nuclei in the raw images by using large-scale computer networks (at the European Molecular Biology Laboratory, EMBL; and Karlsruhe Institute of Technology, KIT) (fig. S4). Image segmentation was performed by (i) recursive refinement of the three-dimensional shapes and internal structures of objects detected in the microscopy data (fig. S5), (ii) subsequent filtering of these objects according to the morphological characteristics expected for nuclei, and (iii) an analysis of the identification rate for each nucleus throughout time (*8*). Because of the high signal-to-noise ratio of the DSLM data, we obtained a robust average segmentation efficiency of 97% during the first 10 hours of embryogenesis and an average of 90% during late gastrulation (*8*). The microscopy data acquired along the two opposing directions were segmented separately and subsequently combined into a complete data set by a fusion algorithm (*8*). A "digital embryo" was derived for each experiment and constitutes a comprehensive database of the positions, sizes, and fluorescence intensities of 92% of the nuclei in the entire embryo (determined by manual controls) (*8*) throughout early embryogenesis from early cleavage stages up to the onset of heartbeat (Fig. 2 and movie S3). The algorithms, furthermore, provide 99.5% efficiency in converting these nuclear positions into migratory tracks, corresponding to one tracking error per 200 time points or 3 to 5 hours (*8*). We processed seven 24-hour time-lapse recordings of zebrafish embryogenesis and obtained developmental blueprints with 55 million nuclear data entries, including a reconstruction of the zebrafish *one-eyed pinhead* mutant (M*Zoep*) (*15*). Our data on zebrafish embryogenesis from 1.5 to 30 hpf are presented as time-lapse movies of the microscopy recordings (movies S2, S4, S7, and S12) and as movies of the reconstructions (movies S3, S5, S8, and S13). Further analysis of the digital embryos (*8*) provides a detailed description of morphogenetic and developmental processes at subcellular resolution (fig. S3), spatiotemporal coordinates and polarity of cell divisions (movie S10 and Fig. 3B and fig. S6), global nuclear population statistics (figs. S3 and S6), embryo-to-embryo variability in morphogenetic key parameters (fig. S7), and cell tracking throughout development (movies S9, S11, S14, and S15 and Fig. 3A).

The digital embryos provide direct quantitative access to a global analysis of cell and tissue behavior, as shown below. In order to visualize morphogenetic domains, we tracked individual cell movements up to somitogenesis stages and color-encoded the information on directionality (movies S9, S14, and S15 and Fig. 3A). This analysis identifies morphogenetic movements during development (emboly, epiboly, convergence, and extension) and provides a global, quantitative perspective of their interplay.

Early morphodynamic symmetry-breaking. Nuclear β-catenin is one of the earliest markers for the future dorsal side of the embryo (~512-cell stage) (*16*, *17*), which raises the question of whether morphodynamic symmetry-breaking also occurs at this early time point. We mapped and analyzed the three-dimensional patterns and polarity of early cell divisions in five embryos during 1.5 to 7 hpf [all experiments were per-

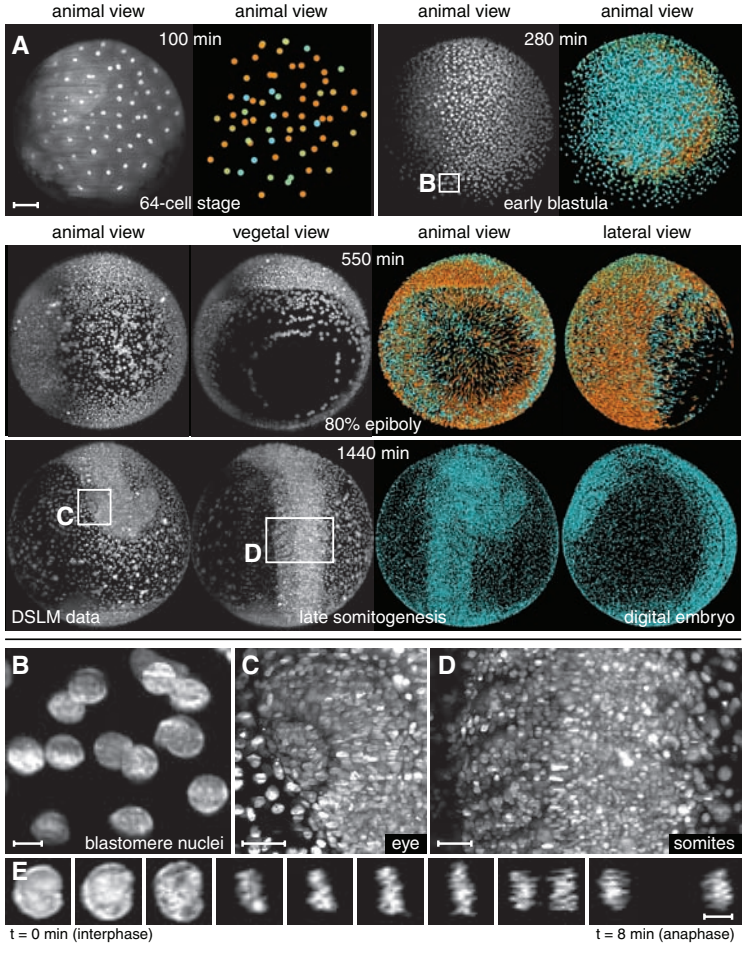

Fig. 2. Imaging and reconstruction of zebrafish embryogenesis. (**A**) Maximum-intensity projections (left) and digital embryo reconstructions (right) of nuclear-labeled wild-type zebrafish embryo (movies S2 and S3) at the indicated times and developmental stages. Color code: movement speeds (0 to 1.2 μm/min, cyan to orange). Images are Lucy-Richardson-deconvolved (10 iterations). Zeiss C–Apochromat 10×/0.45. Scale bar, 100 μm. (**B** to **D** insets and parts) Frames of close-ups on (A), demonstrating subcellular resolution of various areas of the developing embryo. Enlargements scale bar, 10 μm (B), 30 μm (C and D). (**E**) Nuclear morphology of a dividing blastomere from movie S7 (intensity-normalized). Scale bar, 10 μm. *t*, time.

formed at 26.5°C (*13*)] (movie S10). Whereas planes of cell division are evenly distributed [fig. S6b; in contrast to the asymmetry in gastrulation (*18*, *19*)], a symmetry break in the spatiotemporal pattern occurs at the 512-cell stage (movie S10 and Fig. 4A). Initially, cell divisions follow 3-min-long radial waves, originating in the embryonic center. After the 512-cell stage, two circular peripheral waves break this radial symmetry (Fig. 4, A and B, and fig. S8 and movie S10). They occur during division cycles 10 to 13 at an angle that correlates with the future body axis (Fig. 4B).

To investigate whether the break of radial symmetry can also be related to nuclear densities, we determined the nuclear counts in small volumes around the animal pole. This analysis indicates a divergence commencing at 5 hpf, i.e., two hours after the symmetry break in cell division patterns, but still before the morphological signs of shield formation at the onset of convergence (8 hpf) (Fig. 4C). Between 5 and 8 hpf, reduced cell proliferation rates in the future embryonic shield result in lower cell densities dorsally (rather than dorsal compaction) (*20*, *21*) and, thereby, indicate the position of the future body axis.

Thus, by dissecting the three-dimensional pattern of cell divisions in the entire embryo, we reveal an early morphodynamic symmetry break, concomitant with the nuclear localization of β-catenin, that allows an early prediction of the orientation of the body axis, preceding the midblastula transition (*22*).

A model of hypoblast formation. In addition to enabling the analysis of global quantitative studies, the digital embryos allow us to focus on confined morphogenetic events. We investigated the formation of the hypoblast, the inner cell layer, which gives rise to mesoderm and endoderm. The formation of the hypoblast is known to result from internalization of cells (emboly) of the outer layer (epiblast) during gastrulation and stretching and thinning of cell sheets over the yolk (epiboly) (*23*). Our data

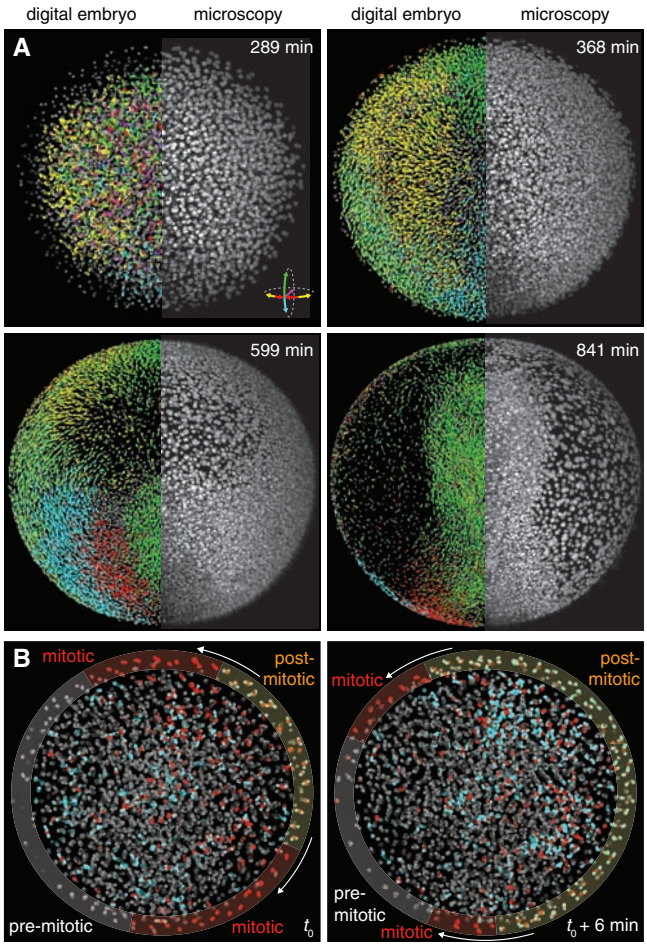

Fig. 3. Cell tracking and detection of cell divisions in the digital embryo. (**A**) Microscopy data (right half of embryo: animal view, maximum projection) and digital embryo (left half of embryo) with color-encoded migration directions (see movie S9). Color code: dorsal migration (cyan), ventral migration (green), toward or away from body axis (red or yellow), toward yolk (pink). (**B**) Dividing cells (red) and their daughter cells (blue). See movie S10 and fig. S6b for complete coverage (1.7 to 6.7 hpf). Yellow, red, and gray overlays indicate progression of the peripheral cell division waves during division cycle 12 (arrows show direction of peripheral waves; t_0 = 216 min, see also Fig. 4).

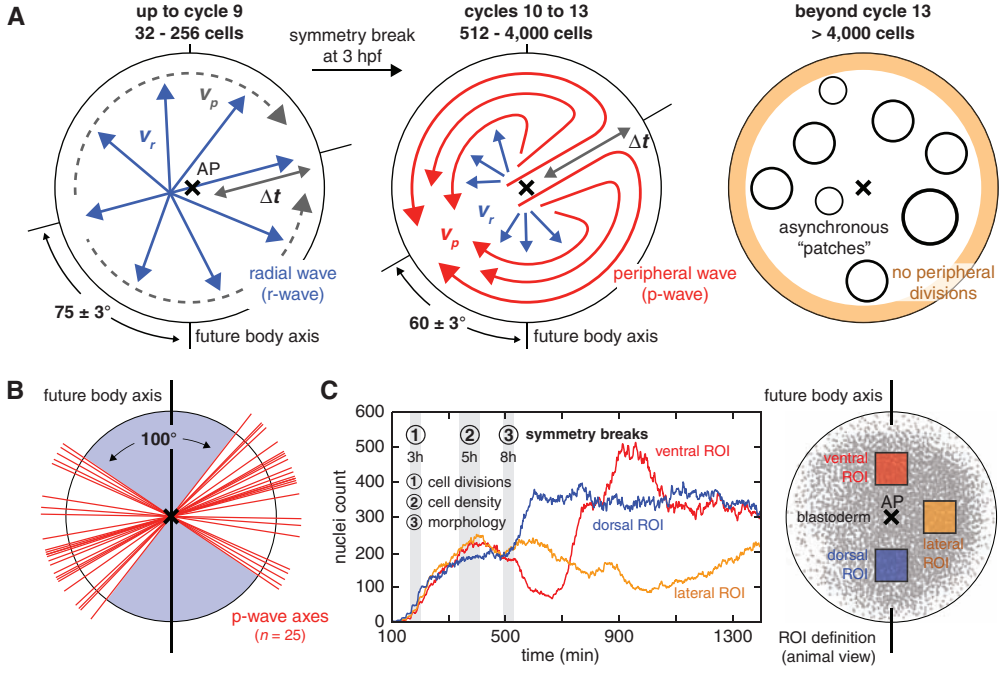

Fig. 4. Symmetry-breaking of the global cell division pattern. (**A**) Illustration of the cell division patterns during early zebrafish embryogenesis: fast radial waves (cycles 1 to 9, progression speed v_r), slow circular peripheral waves (cycles 10 to 13, progression speed v_p), and asynchronous cell-division patches (cycles 14+). Errors are indicated as SEM. A quantification of the parameters v_r, v_p and the time shift Δt between radial and peripheral waves is provided in fig. S8. (**B**) Symmetry axes of 25 peripheral waves (20 slow waves in cycles 10 to 13 and 5 fast waves in cycle 9; n = 5 embryos). Of the 25 waves, 92% occurred at an angle of 45 to 90° to the future body axis. (**C**) Nuclei counts in three 110 by 110 μm^2 domains (future dorsal, ventral, and lateral) reveal the first symmetry break in cell densities at 5 hpf. The symmetry break in the cell division pattern (3 hpf) precedes the symmetry break in cell densities (5 hpf) and the first morphogenetic symmetry break (onset of convergence, 8 hpf).

reveal a pronounced "embolic wave" of internalization and regional differences in modes of internalization (Fig. 5 and fig. S9 and movies S14 and S15).

Starting at 5.8 hpf (40% epiboly at 26.5°C) (*13*) and lasting for 2 hours, ~1550 cells (34% of all cells) internalize around the perimeter of the blastopore to form the mesendoderm (Fig. 5 and fig. S9). After this time window, we did not observe any further cells moving from epiblast to hypoblast.

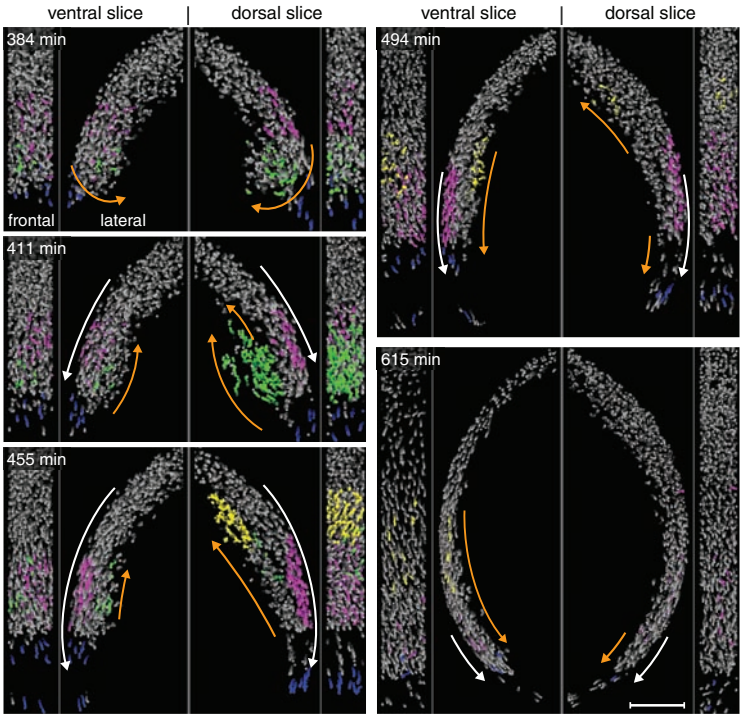

Fig. 5. Mesendoderm internalization and migration in dorsal and ventral hemispheres. Frontal and lateral views of slices on dorsal (shield region, right) and ventral hemispheres (opposite of shield, left). Four cell populations were tracked (movie S16): green or yellow nuclei in the early or late embolic wave, blue nuclei at the leading edge of epiboly, and noninternalizing pink nuclei. Orange and white arrows indicate hypoblast and epiblast cell movements. Scale bar, 100 μm.

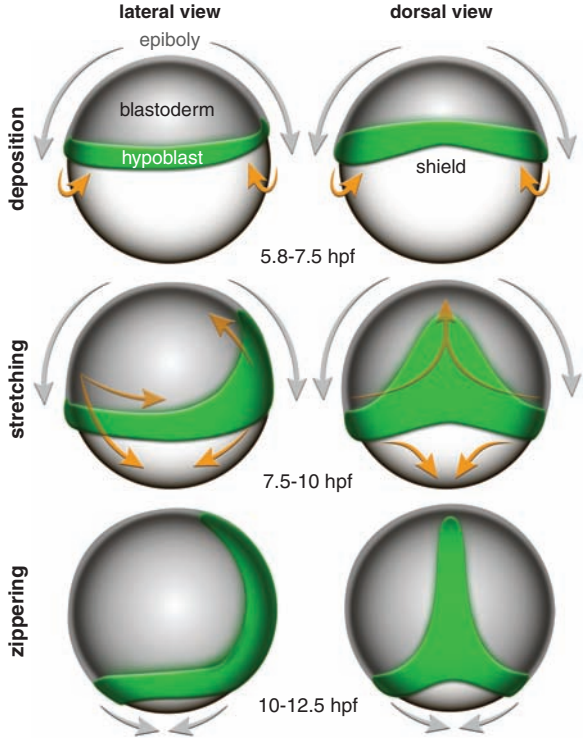

Fig. 6. A model of mesendoderm formation in zebrafish. The hypoblast forms in a single synchronized internalization wave around the entire circumference ("deposition"). On the dorsal side, internalized cells become distributed along the entire future body axis ("stretching"). On the ventral side, the internalized ring of hypoblast cells moves toward the vegetal pole. The ring closes at the vegetal pole ("zippering") and completes the formation of the hypoblast. Orange arrows indicate hypoblast cell movements. Gray arrows indicate epiboly.

Internalizing cells follow the path of a wave, which stretches inward toward the yolk cell, reaches a peak height of 50 μm before rolling over, touches the deep cells situated closer to the animal pole (Fig. 5, green cell population, and movie S16), and completes emboly at 7.5 hpf. Whereas cells internalize around the entire perimeter, the wave is most prominent dorsally. The onset of internalization is synchronized along the blastopore (fig. S9, c and d), but the folding-over at the dorsal shield takes 30 min longer than at other locations along the blastopore. As a consequence of this dorsally pronounced emboly, the dorsal leading edge of epiboly lags behind in its vegetal approach (movie S14).

Modes of internalization (*24*), either involution (synchronously flowing sheets as in amphibian gastrulation) or ingression (cells individually sinking inward), have been subject to intense discussion (*25*, *26*). To determine whether modes of internalization vary regionally, we generated "internalization maps" for the dorsal and ventral hemispheres (fig. S9a). An analysis of time shifts between internalization events around the blastopore reveals that asynchronous internalization and radial intercalation of single cells in the shield region disrupt the internalization pattern on the dorsal hemisphere [fig. S9, b and e; supporting previous single cell–tracking studies (*27*, *28*)]. On the ventral hemisphere, however, mesendoderm internalization occurs exclusively in a synchronous manner (fig. S9, b and e), reminiscent of involution (*24*) or an intermediate mechanism termed "synchronized ingression" (*23*, *29*).

In dorso-anterior regions on the animal hemisphere, internalized cells move antiparallel to epiblast cells toward the animal pole for ~100 min (Fig. 5, purple and yellow cell populations; movie S14). In contrast, internalized cells in the ventral hemisphere change direction within 30 min after internalization and migrate toward the vegetal pole (Fig. 5 and movies S15 and S16).

Unlike gastrulation in *Xenopus* (*30*), a continuous rolling internalization with hypoblast cells moving toward the animal pole does not occur as epiboly proceeds to the vegetal hemisphere (movie S16). Instead, hypoblast cells follow a well-defined leading edge and move parallel to epiblast cells toward the vegetal pole (movie S14, *x*,*z* slice).

A comparative reconstruction of the zebrafish MZ*oep* mutant quantitatively describes its deficiency in forming mesendoderm (*15*, *27*): Whereas ~1550 cells internalize via the embolic wave in the wild-type embryo, the MZ*oep* digital embryo (movies S4 and S5) reveals merely ~60 internalizing cells in the entire embryo during the same time period (movie S6). This visualization shows that the oversized epiblast (*15*) forms through convergence and absence

of internalization and dorsal stretching (movies S5 and S6). Convergence is highly abnormal and prolonged, with ventral cells moving across the animal pole toward the epiblast's center (movie S6).

In conclusion, we show that wild-type hypoblast cells are deposited in a single embolic wave that occurs before epiboly moves the blastopore to the vegetal hemisphere. The embryo is therefore split into a dorso-anterior domain characterized by antiparallel movements of germ layers and a dorso-posterior domain, where the parallel migration of epi- and hypoblast stretches the hypoblast. In the trunk and tail regions, parallel germ layer migration and convergence and/or extension move the mesendoderm, deposited in a ring around the blastopore, to an axial position, closing the blastopore dorsally from anterior to posterior like a zipper.

Our analysis puts previous cell-tracking studies (*31*, *32*) into a global perspective. Regarding mesendoderm formation in zebrafish, a three-stage model is proposed (Fig. 6): Mesendoderm forms by (i) global deposition in a single event, (ii) dorsal stretching, and (iii) anteroposterior "zippering."

Different modes of internalization characterize the initial deposition, with synchronous events (involution and/or synchronized ingression) occurring on the ventral side, and disruption of synchrony (asynchronous ingression and/or radial intercalation) on the dorsal side. Our analysis of the entire embryo describes the migratory behavior of 92% of all cells throughout gastrulation and leads to a comprehensive model that complements and partially revises the general view of zebrafish gastrulation (*30*, *33*). In particular, our finding of a single embolic event contradicts the current assumption of a continuous internalization during epiboly (*30*, *33–35*).

Conclusions. We developed and applied DSLM as a fluorescence microscopy system for the high-speed in vivo observation of embryonic development at subcellular resolution, which enabled cell tracking in the entire early zebrafish embryo. Applying the automated image segmentation pipeline provides a "digital embryo" that visualizes complex developmental events in a global context. We demonstrate application of the method to a quantitative reconstruction of early cell division patterns. This analysis reveals an initial morphodynamic symmetry break, before the onset of zygotic transcription, coinciding with the embryonic body axis. We also follow germ layer formation on a quantitative level and provide a comprehensive model of hypoblast formation in zebrafish embryos. We show that the mesendoderm forms from one-third of the embryo's cells in a single embolic event by means of regionally different modes of internalization.

Our digital embryos constitute complex data sets with information about millions of nuclear positions, as well as thousands of cell tracks and cell divisions per embryo. These data are publicly available in a central repository as a resource for further analyses (*36*).

Detailed recordings of embryonic development will allow the measurement and the modeling of the mechanical forces that drive morphogenesis, e.g., by complementing existing data with information about membrane dynamics. Further applications range from the construction of databases of organ development (using tissue-specific fluorescent lines) and the analysis of mutant phenotypes (*37–39*) to the quantification of the variability of vertebrate cell lineages. Moreover, with its high-throughput and high-content capabilities DSLM presents a powerful tool for systems biology and enables complete in vivo reconstructions of gene expression dynamics that incorporate the steadily growing number of gene and enhancer trap lines (*40–42*). In addition, DSLM should be suitable for analyses of entire mouse, chicken, and *Xenopus* early embryogenesis—the unfavorable light-scattering tissue properties of *Xenopus* can be partially overcome by DSLM's intrinsic structured illumination and multiview imaging capabilities. The comparison of individuals within species and across species borders might allow us to reveal the conserved and emerging morphogenetic rules of embryogenesis.

References and Notes

1. J. E. Sulston, E. Schierenberg, J. G. White, J. N. Thomson, *Dev. Biol.* **100**, 64 (1983).
2. P. Lemaire, *Science* **312**, 1145 (2006).
3. Y. Hirose, Z. M. Varga, H. Kondoh, M. Furutani-Seiki, *Development* **131**, 2553 (2004).
4. M. Rembold, F. Loosli, R. J. Adams, J. Wittbrodt, *Science* **313**, 1130 (2006).
5. S. J. England, G. B. Blanchard, L. Mahadevan, R. J. Adams, *Development* **133**, 4613 (2006).
6. S. G. Megason, S. E. Fraser, *Cell* **130**, 784 (2007).
7. R. Y. Tsien, L. Ernst, A. Waggoner, in *Handbook of Biological Confocal Microscopy*, J. B. Pawley, Ed. (Springer, New York, 2006), pp. 338–352.
8. Materials and methods are available as supporting material on *Science* Online.
9. J. Huisken, J. Swoger, F. Del Bene, J. Wittbrodt, E. H. Stelzer, *Science* **305**, 1007 (2004).
10. P. J. Keller, F. Pampaloni, E. H. Stelzer, *Curr. Opin. Cell Biol.* **18**, 117 (2006).
11. P. J. Keller, F. Pampaloni, E. H. Stelzer, *Nat. Methods* **4**, 843 (2007).
12. M. A. Neil, R. Juskaitis, T. Wilson, *Opt. Lett.* **22**, 1905 (1997).
13. K. K. Hisaoka, H. I. Battle, *J. Morphol.* **102**, 311 (1958).
14. T. Kanda, K. F. Sullivan, G. M. Wahl, *Curr. Biol.* **8**, 377 (1998).
15. K. Gritsman *et al.*, *Cell* **97**, 121 (1999).
16. S. Schneider, H. Steinbeisser, R. M. Warga, P. Hausen, *Mech. Dev.* **57**, 191 (1996).
17. S. T. Dougan, R. M. Warga, D. A. Kane, A. F. Schier, W. S. Talbot, *Development* **130**, 1837 (2003).
18. M. L. Concha, R. J. Adams, *Development* **125**, 983 (1998).
19. Y. Gong, C. Mo, S. E. Fraser, *Nature* **430**, 689 (2004).
20. R. M. Warga, C. Nusslein-Volhard, *Dev. Biol.* **203**, 116 (1998).
21. B. Schmitz, I. A. Campos-Ortega, *Rouxs Arch. Dev. Biol.* **203**, 374 (1994).
22. D. A. Kane, C. B. Kimmel, *Development* **119**, 447 (1993).
23. L. Solnica-Krezel, *Curr. Biol.* **15**, R213 (2005).
24. J. P. Trinkaus, *Cells into Organs: The Forces That Shape the Embryo* (Prentice-Hall, Englewood Cliffs, NJ, ed. 2, 1984).
25. D. Kane, R. J. Adams, in *Pattern Formation in Zebrafish*, L. Solnica-Krezel, Ed. (Springer, Heidelberg, 2002).
26. L. A. Rohde, C. P. Heisenberg, *Int. Rev. Cytol.* **261**, 159 (2007).
27. J. A. Montero *et al.*, *Development* **132**, 1187 (2005).
28. J. Shih, S. E. Fraser, *Development* **121**, 2755 (1995).
29. R. J. Adams, C. B. Kimmel, in *Gastrulation: From Cells to Embryo*, C. D. Stern, Ed. (Cold Spring Harbor Laboratory Press, Cold Spring Harbor, NY, 2004), pp. 305–316.
30. L. Wolpert, *Principles of Development* (Oxford Univ. Press, New York, ed. 3, 2007).
31. D. C. Myers, D. S. Sepich, L. Solnica-Krezel, *Dev. Biol.* **243**, 81 (2002).
32. D. S. Sepich, C. Calmelet, M. Kiskowski, L. Solnica-Krezel, *Dev. Dyn.* **234**, 279 (2005).
33. S. F. Gilbert, *Developmental Biology* (Sinauer Associates, Sunderland, MA, ed. 8, 2006).
34. R. M. Warga, C. B. Kimmel, *Development* **108**, 569 (1990).
35. G. Pezeron *et al.*, *Curr. Biol.* **18**, 276 (2008).
36. Movies and zebrafish digital embryos can be downloaded at www.embl-heidelberg.de/digitalembryo
37. D. A. Kane *et al.*, *Development* **123**, 47 (1996).
38. C. P. Heisenberg, M. Tada, *Semin. Cell Dev. Biol.* **13**, 471 (2002).
39. D. S. Sepich, L. Solnica-Krezel, *Methods Mol. Biol.* **294**, 211 (2005).
40. S. Ellingsen *et al.*, *Development* **132**, 3799 (2005).
41. S. Parinov, I. Kondrichin, V. Korzh, A. Emelyanov, *Dev. Dyn.* **231**, 449 (2004).
42. K. Asakawa *et al.*, *Proc. Natl. Acad. Sci. U.S.A.* **105**, 1255 (2008).

43. We thank U. Liebel, M. Alef, and M. Wahlers for excellent KIT/EMBL computer cluster support; the EMBL mechanical workshop for custom hardware; A. Riedinger and G. Ritter for custom electronics; F. Härle and A. Riedinger for custom microscope operating software; W. Dilling for technical drawings; M. Knop, K. Brown, K. Khairy, J. Martinez, D. Gilmour, and C.-P. Heisenberg for critical manuscript comments; L. Centanin for immunostained medaka embryos; C.-P. Heisenberg for MZ*oep* mutants; S. Terjung for Leica SP5 support; G. Giese for Zeiss LSM 510 NLO support. Financial support: EU-FP6-STREP Plurigenes, DFG SFB-488 (J.W.); Studienstiftung des deutschen Volkes (P.J.K.); Hartmut Hoffmann-Berling International Graduate School of Molecular and Cellular Biology, HBIGS (A.D.S.). Contributions: P.J.K. outlined the digital embryo project, designed and built the DSLM, recorded the microscopy data, developed the image processing pipeline, performed the reconstructions and drafted the manuscript. A.D.S. developed the biological methods, performed the biological preparations, contributed to project planning and participated in the writing of the manuscript. E.H.K.S. outlined the DSLM development, cosupervised the project, and participated in manuscript preparation. P.J.K., A.D.S., and J.W. analyzed the digital embryos. J.W. guided the biological research, cosupervised the project, and participated in the writing of the manuscript.

Supporting Online Material

www.sciencemag.org/cgi/content/full/1162493/DC1
Materials and Methods
Figs. S1 to S9
References
Movies S1 to S16

30 June 2008; accepted 1 October 2008
Published online 9 October 2008;
10.1126/science.1162493
Include this information when citing this paper.